Editors' Suggestion

Low-Frequency Quantum Sensing

E.D. Herbschleb,[1,*] I. Ohki,[1,2] K. Morita,[1] Y. Yoshii,[3] H. Kato,[4] T. Makino,[4] S. Yamasaki,[5] and N. Mizuochi[1,6,†]

[1] *Institute for Chemical Research, Kyoto University, Gokasho, Uji-city, Kyoto 611-0011, Japan*
[2] *Institute for Quantum Life Science, National Institutes for Quantum Science and Technology, Chiba 263-8555, Japan*
[3] *Sumida Corporation, KDX Ginza East Building 7F, 3-7-2, Irifune, Chuo-ku, Tokyo 104-0042, Japan*
[4] *National Institute of Advanced Industrial Science and Technology (AIST), Tsukuba, Ibaraki 305-8568, Japan*
[5] *Kanazawa University, Kanazawa, Ishikawa 920-1192, Japan*
[6] *Center for Spintronics Research Network, Kyoto University, Uji, Kyoto 611-0011, Japan*

(Received 30 March 2022; revised 13 June 2022; accepted 2 August 2022; published 22 September 2022)

Exquisite sensitivities are a prominent advantage of quantum sensors. Ramsey sequences allow precise measurement of direct current fields, while Hahn-echo-like sequences measure alternating current fields. However, the latter are restrained for use with high-frequency fields (above approximately 1 kHz) due to finite coherence times, leaving less-sensitive noncoherent methods for the low-frequency range. In this paper, we propose to bridge the gap with a fitting-based algorithm with a frequency-independent sensitivity to coherently measure low-frequency fields. As the algorithm benefits from coherence-based measurements, its demonstration with a single nitrogen-vacancy center gives a sensitivity of 9.4 nT $\mathrm{Hz}^{-0.5}$ for frequencies below about 0.6 kHz down to near-constant fields. To inspect the potential in various scenarios, we apply the algorithm at a background field of tens of nTs, and we measure low-frequency signals via synchronization.

DOI: 10.1103/PhysRevApplied.18.034058

I. INTRODUCTION

Quantum sensing promises high-resolution sensors with unparalleled sensitivities by working with quantum properties such as coherence [1]. Nitrogen-vacancy (N-V) centers in diamond are high-potential candidates as such sensors for their extraordinary quantum mechanical properties even at room temperature [1,2], including long spin-coherence times [3,4]. In conventional ac field-detection techniques with Hahn-echo and dynamical-decoupling schemes, the phase-accumulation time for the highest sensitivity is at around $T_2/2$ [3], which dictates the lowest frequency measurable with high sensitivity. For frequencies far from $2T_2^{-1}$, the sensitivity becomes significantly worse. For higher frequencies, detection schemes have been proposed and demonstrated in the GHz range [5,6]. On the other hand, the lowest frequency detected with a Hahn-echo sequence is 833 Hz, as demonstrated with the longest T_2 [3]. Moreover, there is a significant amount of work focusing on dc sensing with optically detected magnetic resonance (ODMR) measurements, which, although generally not specifically investigated, is envisaged to work for some low frequencies as well [7–12].

Low-frequency sensing with high sensitivity is required for many applications. For example, it is useful for chemical structure analysis [13,14] and for searching particles beyond the standard model [15,16] with low-field nuclear magnetic resonance (NMR) measurements. Contrary to NMR at high fields, at low fields, J couplings, electron-mediated scalar couplings between spins in a molecule, are strongly represented. Since these are highly sensitive to the electronic structure of a molecule and its geometry, low-field spectra tend to be rather different for each molecule, while the differences in chemical shifts dominating at high fields could be small [13,14]. Moreover, since the inhomogeneous line width is proportional to the field strength, at low fields the line width and the signal-to-noise ratio improve significantly [17]. Additionally, in conventional high-field NMR, resonant frequencies can be shifted down into the audiofrequency range (kHz and below), because this conversion enables filtering of high-frequency noise, and this is the region with high sensitivity for the phase detector [18,19].

Previously, low-frequency-like fields have been measured with cw ODMR techniques [7–12]. However, a drawback is the limited sensitivity compared to pulsed techniques, which becomes worse with longer coherence times [20]. Alternatively, a pulsed-ODMR technique was proposed, which removes the laser-induced

*herbschleb@dia.kuicr.kyoto-u.ac.jp
†mizuochi@scl.kyoto-u.ac.jp

power broadening and as such improves the sensitivity significantly, although it is not as sensitive as coherence-based sequences still [20].

For sensing at zero and ultralow fields, recently a cw ODMR technique was applied for an ensemble of N-V centers, measuring at a field below approximately 3 μT [21]. The insensitivity normally expected for such techniques at low field was countered by applying circularly polarized microwave fields, which mostly affect one of each energy-level pair; the levels in each pair cross at zero field. In an alternative theoretical approach, a three-level system control was applied, which required a low bias field ($\leq$ 20 G [22]).

In the following, we present a fitting-based algorithm to measure low-frequency ac magnetic fields. With simulations and measurements, we explore the features of this algorithm; in principle, any low-frequency periodic field can be measured. We show that for low frequencies, which is below about $(2T_2^*)^{-1}$, the sensitivity of this algorithm is independent of frequency. Moreover, we employ the algorithm at a rather low background field to investigate the feasibility at such fields. Finally, we demonstrate the technique with synchronized low-frequency signals. Single N-V centers at room temperature are used for all experiments.

II. RESULTS

A. Algorithm

The quantum measurement utilized in the algorithm is the free-induced decay (FID) sequence [23], as displayed in the inset of Fig. 1(a). If the microwave (MW) frequency of the $\pi/2$ pulses is set exactly to the energy difference between the $m_s = 0$ and $m_s = \pm 1$ states, as appearing in ODMR spectra [24] [Fig. 1(a)], the phase of the spin does not change during the time delay between the $\pi/2$ pulses. However, when a field is applied during this delay, the phase of the spin changes. For example, depending on the magnitude of an applied dc magnetic field, the spin rotates along the z axis, which results in an oscillation in readout signal [see, for example, Fig. 1(c)].

As illustrated in Fig. 1(b), in this algorithm, the sequence to measure a low-frequency ac field consists of

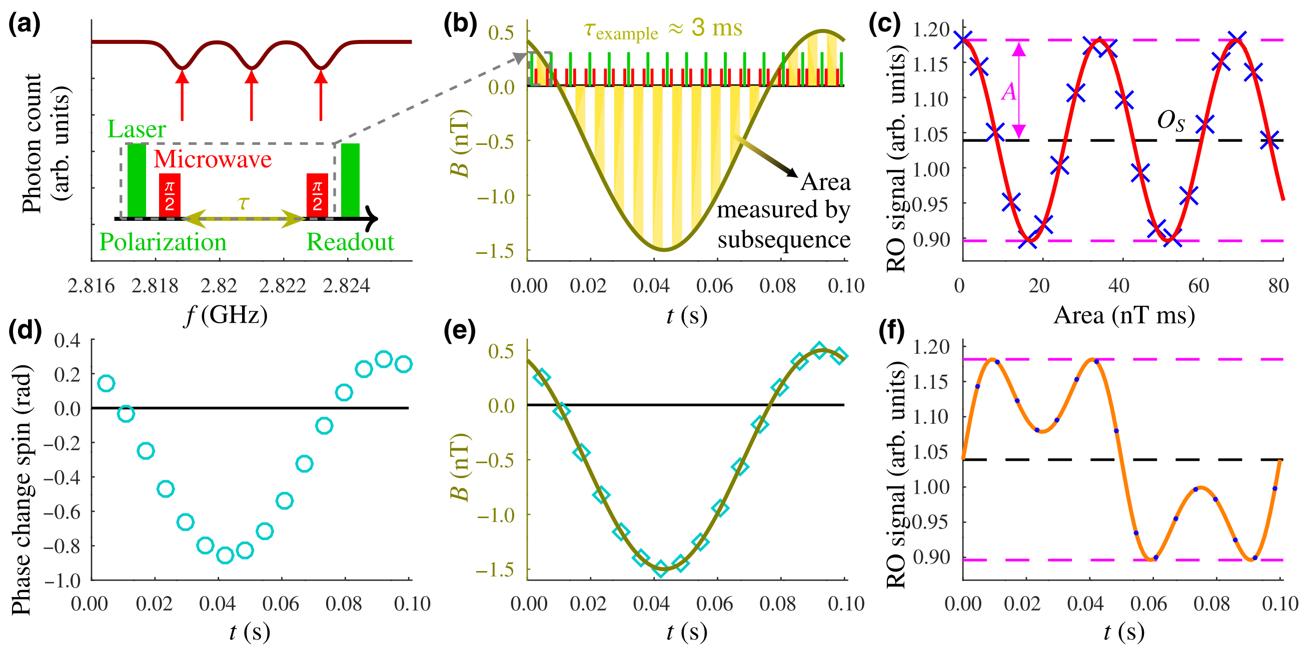

FIG. 1. Algorithm. (a) Illustrative ODMR spectrum (dark red line at the top) with three valleys (indicated with red arrows) related to the energy differences between the $m_s = 0$ and $m_s = -1$ states with hyperfine splitting due to the ^{14}N nucleus. The inset shows the basic pulse sequence for FID measurements with delay τ between the MW $\pi/2$ pulses. (b) In the algorithm, a fixed-delay FID sequence is repeated during the period of the signal, measuring the yellow areas. Thus, the sequence functions as an oscilloscope with quantum measurements. (c) For a single sequence with the same fixed delay, by applying a dc field the spin rotates around the z axis depending on the size of the area (here the dc field magnitude times the fixed delay), resulting in an oscillation of the readout (RO) signal (simulation results with blue crosses, fit with red line). Such a measurement can be used as calibration, for example for the amplitude A (magenta dashed lines are the extrema) and the offset O_S (black dashed line) from Eq. (1). (d) The final phase of the spin (analyzed simulation results with cyan circles) depends on the measured area during each subsequence. (e) By taking the shape of the areas into account while fitting, the parameters such as the ac field amplitude are retrieved (analyzed simulation results with cyan diamonds, resulting field with olive line). (f) With a single FID sequence the result would be ambiguous for larger fields given the rotational symmetry of the phase. However, the combination of multiple sequences allows some of this information to be retained (simulation results with blue dots, fit with orange line).

repetitions of fixed-delay FID subsequences within the period of the field, which can be accumulated to obtain a sufficiently significant signal. Essentially, this is similar to a classical oscilloscope (with averaging), but with quantum measurements instead (which suggests the name "QScope"), and the principle of repeating measurements is quite common, an example with N-*V* centers is with ODMR spectra [8]. For the resulting series of data points, each data point with readout signal S follows from

$$S = A\sin(\omega \int B(t)\,dt + \theta) + O_S, \quad (1)$$

where A is the amplitude, ω the frequency, θ the phase, and O_S the offset of the oscillation in the signal, which stems from the magnetic field B that rotates the spin. The parameters of this function are calibration constants (as explained in Sec. I within the Supplemental Material [27]), which follow from a calibration measurement giving a result as in Fig. 1(c), or they can be computed directly from the N-*V* center's parameters (T_2^*) and the time delay [3]. For a sinusoidal ac field, the magnetic field B at each time t is given by

$$B = B_{\text{ac}}\sin(2\pi f t + \phi) + B_{\text{dc}}, \quad (2)$$

with B_{ac} the field amplitude, f its frequency, ϕ the phase, and B_{dc} the constant field offset. Thus to find the ac field amplitude, this algorithm relies on fitting the data points of each subsequence to find the fitting parameter B_{ac}.

However, the field at each data point is not found directly, as the readout signal only gives the final phase of the spin at the end of each subsequence, as plotted in Fig. 1(d). To retrieve the measured field accurately, the shape of the field during the subsequence needs to be taken into account, as implied by the integral in Eq. (1). By fitting the readout signal directly utilizing integrals, the field is retrieved accurately [Fig. 1(b,e)].

In Fig. 1(f), a directly fitted readout signal is plotted. This illustrates an additional advantage of the algorithm, which is an inherent increase in dynamic range for ac fields. This is a consequence of the relatively slow increase of field over time, which allows us to determine how often the spin rotated fully by 2π at the extrema of the ac field. Generally, multiple measurements have the ability to increase the dynamic range [25].

Any periodic function can be fitted, though one requirement out of two is necessary to perform the measurement: either the period of the signal needs to be known, or a way of synchronization must exist, for example via triggered measurements. The remainder of the parameters results from the measurement, for example, in Fig. 1(e) the phase and dc component of the sinusoid are found as well. Throughout this paper, the main focus is on measuring low-frequency ac fields. In other words, we measure the amplitude, the result of which is independent of parameters such as the phase and the dc component.

B. Sensitivity definition

The sensitivity of a measurement is its uncertainty times the square root of the measurement time [3,26]. Therefore, for this fitting-based algorithm, the sensitivity η_{coef} of each fitting coefficient coef is

$$\eta_{\text{coef}} = \sigma_{\text{coef}}\sqrt{T_{\text{meas}}}, \quad (3)$$

with σ_{coef} the uncertainty of the respective fitting coefficient, and T_{meas} the measurement time. The σ_{coef} follows from fitting the measurement data, which allows computation of the standard error (uncertainty) of the fitting coefficients.

The sensitivity depends on the time delay between the $\pi/2$ pulses in the sequence. The optimum is derived in Sec. I within the Supplemental Material [27]. At first, the linear regime is investigated, since the sensitivities given by Hahn-echo measurements are based on a single point (at the maximum gradient), which is the linear regime. Moreover, the sensitivity of ODMR techniques is based on the maximum gradient of a valley in the ODMR spectrum [Fig. 1(a)], which is the linear regime as well. Therefore, this allows a fair comparison with these standard methods.

C. Measurement

The sample measured throughout this paper consists of *n*-type diamond. It is epitaxially grown onto a Ib-type (111)-oriented diamond substrate by microwave plasma-assisted chemical-vapor deposition with enriched ^{12}C (99.998%) and with a phosphorus concentration of approximately 5×10^{16} atoms cm^{-3} [3,28]. We target individual electron spins residing in single N-*V* centers with a standard in-house built confocal microscope; each set of experiments works with a different N-*V* center, as locations are lost in between experiments. MW pulses are applied via a thin copper wire. Since the nitrogen atom causes hyperfine splitting of the $m_s = \pm 1$ states, to ensure maximum contrast in our measurements, each energy difference is addressed with a separate MW source [so imagine all three frequencies indicated by arrows in Fig. 1(a) are applied], unless stated differently. Magnetic fields are induced with a coil near the sample. All experiments are conducted at room temperature.

N-*V* centers with longer inhomogeneous dephasing times (T_2^*) are more beneficial for the sensitivity of coherence-based sensors, therefore, a center with a T_2^* of about 1 ms is chosen for the initial experiments [see Fig. 2(a)]. Although the optimum time delay is about $T_2^*/2$ (Sec. I within the Supplemental Material [27]), a slightly shorter time delay is applied. The reason is that while the sensitivity is not significantly worse for delays near the

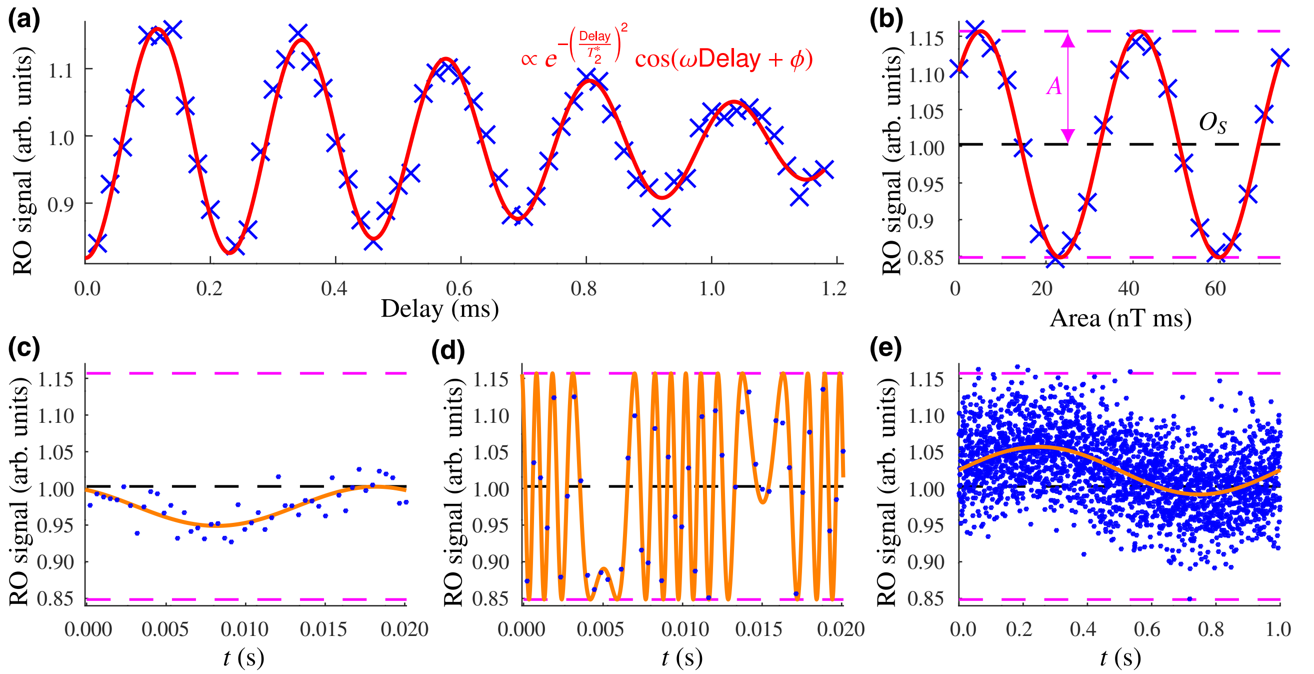

FIG. 2. Exploratory measurements. (a) RO signal versus delay giving the FID measurement result (data with blue crosses, fit with red line) to determine T_2^* ($1.05^{+0.05}_{-0.05}$ ms). (b) Calibration measurement for a delay of 0.4 ms (data with blue crosses, fit with red line). The horizontal black dashed line indicates the offset O_S, while the horizontal magenta dashed lines give the extrema due to amplitude A [see Eq. (1)]. (c) Example measurement exhibiting the independence of phase and offset when measuring an ac field (50-Hz signal with an amplitude of 3.1 nT, data with blue dots, fit with orange line). (d) Example measurement for a high dynamic range measurement, which is outside the linear regime (data with blue dots, fit with orange line). The amplitude is 100 times the amplitude in (c) and (e). (e) Example measurement for a field of 1 Hz with an amplitude of 3.1 nT (data with blue dots, fit with orange line). The offset field of the N-V center for the measurements in this figure is about 1.8 mT.

optimum, the apparent T_2^* of a measurement decreases with measurement time due to environmental effects [3]. So even though the actual T_2^* of the N-V center is longer than 1 ms (see Sec. II within the Supplemental Material [27]), since long measurements are required to accurately estimate the sensitivities for low frequencies, the apparent T_2^* might be less for these measurements. Hence, we choose a time delay of 0.4 ms, since it ensures a sensitivity within 10% of the optimum for the considered range of apparent T_2^*s (see Fig. S2 within the Supplemental Material [27]).

First, the algorithm principles described in the previous section are elucidated with example measurements. The calibration data, equivalent to Fig. 1(c), are depicted in Fig. 2(b). The contrast with a time delay of 0.4 ms is close to 30%, as expected with $T_2^* \approx 1$ ms. In Fig. 2(c), a sinusoid with nonzero phase and dc component is measured to demonstrate the independence of such parameters for getting the ac amplitude, here 3.1 nT. The measurement of a signal with an amplitude beyond the standard dynamic range (of a single-sequence measurement), shown in Fig. 2(d), illustrates the increase of the dynamic range by measuring a signal with an amplitude of 0.31 μT. Finally, Fig. 2(e) plots a measurement result for the lowest frequency measured (1 Hz) with an amplitude of 3.1 nT. This visualizes that a large number of data points, although with significant individual spread, indeed resemble accurately the ac field.

D. Sensitivity measurement

To inspect the performance of the algorithm, the sensitivity is calculated and measured for a range of frequencies. Since the measurement time [see Eq. (3)] follows from the period of the signal (period duration times number of accumulations), this is a proper figure of merit, which includes all overhead time. Moreover, it allows comparison with the standard Hahn-echo measurement. For the latter, to look at its best possible sensitivity, we ignore its overhead time. However, the disadvantage in the comparison for our algorithm is rather small, since at low frequencies, the overhead time of the standard Hahn-echo measurement would be negligible. As additional comparisons, we compute the theoretically best pulsed ODMR sensitivity for the measured N-V center [20,26], the averaged sensitivity over low frequencies for the longer measurement times by fitting a Lorentzian in the Fourier spectrum [29], and the dc-field sensitivity of the cw ODMR technique for our sample [20].

The calculated sensitivity, explained in more detail in Secs. I and III within the Supplemental Material [27], is drawn in Fig. 3(a). This shows that the sensitivity is

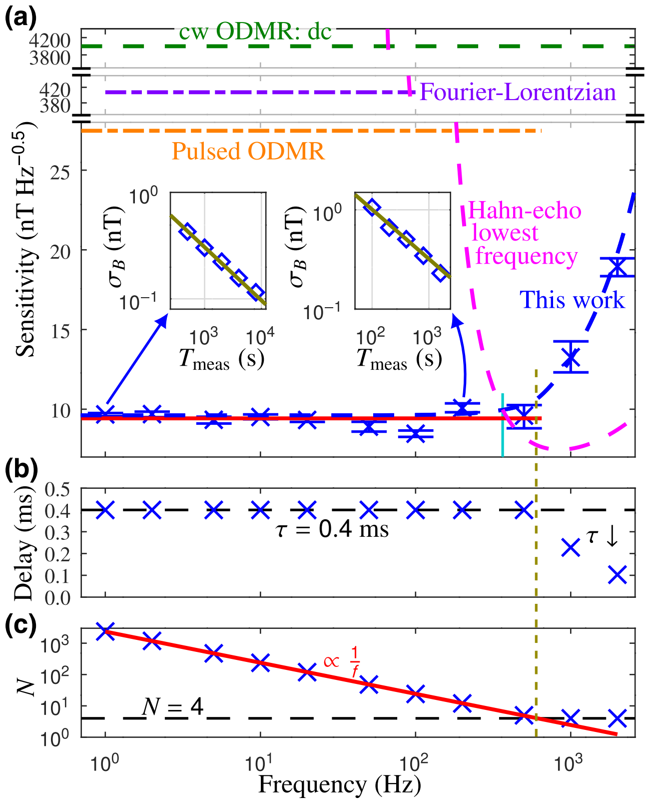

FIG. 3. Sensitivity. (a) Sensitivity versus frequency: data points with blue crosses (error bars indicate standard errors); calculated result with blue dashed line; fitted result for low frequency with horizontal red line ($\eta_{ac} = 9.4^{+0.1}_{-0.2}$ nT Hz$^{-0.5}$); calculated result with Hahn-echo sequence for the current longest T_2 with magenta dashed line (adjusted from Ref. [3] with the parameters of the current experimental setup for fair comparison); calculated result for optimal pulsed ODMR [20] with orange dashed-dotted line; averaged result over low frequencies for Fourier-Lorentzian as a guide to the eye with purple dashed-dotted line; calculated result for dc sensing via cw ODMR as a guide to the eye with green dashed line at the top (for the current N-V center and experimental setup, adjusted from Ref. [20]); threshold frequency with vertical cyan line ($f_{threshold}$ = 0.36 kHz). Insets show two examples of the amplitude uncertainty versus measurement time T_{meas} results (data with blue diamonds, fits with olive lines), where fits give the sensitivities (left for 1 Hz and right for 0.2 kHz). Note the breaks on the vertical axis. Here, the offset field of the N-V center is about 1.8 mT. (b) The fixed delay applied in the subsequences for each frequency (blue crosses), with a maximum of 0.4 ms (horizontal black dashed line). For high frequencies, this delay decreases since a minimum number of data points are required per period. (c) Number of subsequences N (blue crosses, fit with red line) per period, thus data points, for each frequency, with a minimum of 4 (horizontal black dashed line). The vertical olive dashed line is a guide to the eye at the maximum frequency where $N > 4$.

expected to be frequency independent below a certain threshold frequency (see Sec. III within the Supplemental Material [27]). This is sensible, since when halving the frequency, the period and hence measurement time doubles, but the number of data points N also doubles. Since $\eta \propto T_{meas}^{0.5}$ and $\eta \propto \sigma_{coef} \propto N^{-0.5}$, the sensitivity is constant. Above the threshold, the sensitivity becomes worse simply because at least several data points are required in one period of the signal [see Fig. 3(c)]; four are chosen here for fitting the four unknowns of the current signal shape. Compared to Nyquist's sampling theorem, which states that the signal must be sampled at a rate over 2 times the highest frequency component in order to reconstruct it faithfully, a higher sampling rate is required, since we look at a finite time of a single period only. Either way, it is reflected by the measurements at higher frequencies, where the time delay between the MW pulses decreases linearly to maintain a sufficient number of points [with the period of the signal, see Fig. 3(b)], and hence the sensitivity worsens (roughly proportional to $T_{period}^{-0.5}$, until the overhead time becomes significant). Moreover, for the highest two frequencies (which are outside the studied low-frequency regime), multiple periods are measured, as fitting four unknowns on four data points is often mathematically possible, but having more data points than parameters is preferred for fitting.

The uncertainty σ_{ac} is measured for a number of measurement times for frequencies ranging from 1 Hz to 2 kHz, and the results are fitted to Eq. (3) to determine the sensitivity for each frequency [see insets of Fig. 3(a)]. The results are added to Fig. 3(a); they are consistent with the calculated results. The low-frequency sensitivity is $9.4^{+0.1}_{-0.2}$ nT Hz$^{-0.5}$. For lower frequencies, the sensitivities become slightly worse, which we attribute to the earlier mentioned decay of the apparent T_2^*, since determining the sensitivities for these frequencies takes more time. The results and explanations for the other fitting parameters are given in Sec. IV within the Supplemental Material [27].

E. Low-field measurement

Measuring at low field adds the complexity of level (anti)crossings, which could render a sensor insensitive. Therefore, to investigate the algorithm at low fields, first, we cancel the field in the z direction to below approximately 1 nT, as explained in detail in Sec. V within the Supplemental Material [27], which results in overlapping energy levels of the positive and negative spin states. For the sensing experiment, instead of the previous three MWs, we use a single MW for the lower-frequency transition only. We set the frequency of this MW to the energy difference at zero field. Now, if any magnetic field is applied, the two overlapping energy levels change equally in opposite directions. Thus, as long as the final MW pulse in each FID sequence is along the same axis as the preparation

MW pulse, both possible states have the same effect on the readout signal, even though their spins rotate in opposite directions effectively [see Fig. 4(d,e)].

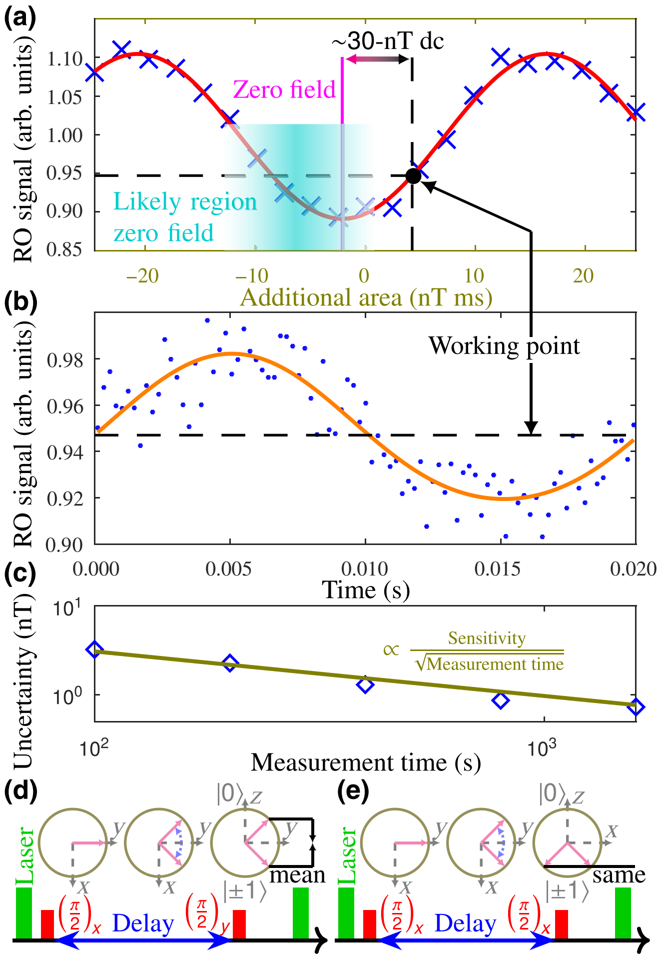

FIG. 4. Low-frequency sensing at low field. (a) Calibration measurement for a delay of 0.2 ms around zero field (RO signal is readout signal, data with blue crosses, fit with red line). The cyan-shaded area indicates the range of fields that include the actual zero field based on FID measurements (Sec. V within the Supplemental Material [27]), while the extremum (vertical magenta line) in this region is when the additional field cancels the remaining background field exactly. The measurements in (b) and (c) are performed at a background field of 30 nT (black dashed lines). (b) Example measurement for a field of 50 Hz with an amplitude of 10 nT at a background field of 30 nT (data with blue dots, fit with orange line). (c) Uncertainty versus measurement time to find the sensitivity for the same signal as in (b) (data with blue diamonds, fit with olive line). (d) Near zero field, when the preparation MW pulse (first lower red rectangle after the laser pulse), here $(\pi/2)_x$, and the readout MW pulse, here $(\pi/2)_y$, are along different axes, the result depends on the spin state and roughly averages towards a field-independent value (black arrows). (e) When the readout MW pulse is along the same axis, here $(\pi/2)_x$, the readout result is the same (black line) for each spin state, enabling measurement of the field.

To measure a low-frequency field, the background field needs to remain sufficiently constant during the measurement; for example, the daily fluctuation in the earth magnetic field is in the order of tens of nTs [30]. To limit the measurement time, we choose a frequency of 50 Hz and we use a delay of 0.2 ms. The calibration measurement is displayed in Fig. 4(a), for which the background field is close to 0 T. FID measurements locate the zero field within a range of tens of nTs, such that the valley in the calibration measurement in this range gives the actual zero field, here with a precision of 0.7 nT (see Supplemental Material V [27]).

For the low-frequency measurement, instead of measuring at exact zero, we measure closer to the linear regime, resulting in a background field of ~ 30 nT. An example measurement is plotted in Fig. 4(b); the slight asymmetry around the center horizontal indicates that we are at the edge of the linear regime. At this background field, we measure the sensitivity, which is 31^{+1}_{-1} nT $\text{Hz}^{-0.5}$ [Fig. 4(c)]. This low-field sensitivity is worse compared to the high-field sensitivity, mostly owing to the 2 times shorter time delay and the single-tone MW (instead of multitone), and to a lesser degree owing to the lower coherence time of the measured N-V center, the vicinity of the nonlinear regime, and a nonperfect detuning (Sec. V within the Supplemental Material [27]).

F. Synchronized measurement

So far we study signals with a known period, but as mentioned in Sec. II A, an alternative is measuring synchronized signals, such as NMR signals. To obtain an example low-frequency NMR signal, the sample (water or ethanol) is placed inside a permanent magnet (approximately 1 T) at room temperature, and with a rf $\pi/2$ pulse emitted via a coil around the sample, its nuclear spins are excited. This pulse marks the synchronization time. The transient emitted field, so here its free nuclear precession response, is picked up via the same coil, which is connected to the coil around the N-V center via a switch in order to record it by the N-V center. Owing to mixing the emitted signal with a reference oscillator, a down-converted low-frequency signal is obtained (see the Appendix for details). Since the signals decay and thus a large difference in amplitude between the start and the end exists, a delay of 0.1 ms is chosen to allow higher amplitudes to fit the linear regime, while also easing the environmental effects given the required long measurements [3], reducing the sensitivity by less than 2 times compared to the initial measurements (Figs. 2 and 3).

For the straightforward case of deionized water, the result is plotted in Fig. 5(a). A low-frequency signal of about 7 Hz is measured, the amplitude of this signal decays from 43.7 to 2.5 nT in 0.35 s due to the inhomogeneous dephasing time $T_2^* \approx 0.2$ s. On the other hand, ethanol has

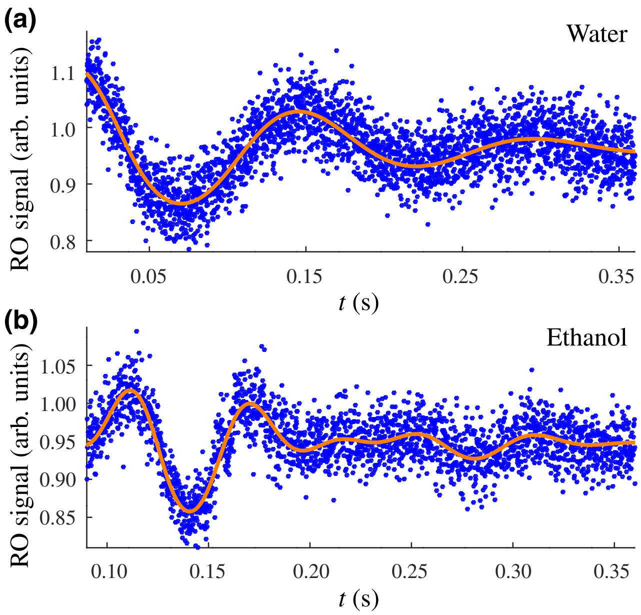

FIG. 5. Synchronized low-frequency sensing. (a) Free nuclear precession RO signal versus time for part of the time axis (total length is 1.0 s, repeated 10 000 times, data with blue dots, fit with orange line) measuring the response of a deionized water sample after applying a rf $\pi/2$ pulse. Here, the amplitude of the low-frequency signal (7 Hz) starts at 43.7 nT (left side), and decays to 2.5 nT (right side). (b) Free nuclear precession readout signal versus time for part of the time axis (total length is 1.0 s, repeated 20 000 times, data with blue dots, fit with orange line) measuring an ethanol sample after applying a rf $\pi/2$ pulse. Here, the amplitudes of the low-frequency signal start at 9.6 nT (7 Hz), 19.7 nT (14 Hz), and 13.6 nT (21 Hz), and decay to 0.4 nT, 0.9 nT, and 0.6 nT, respectively. The offset field of the N-V center for the measurements in this figure is about 0.5 mT.

a more involved spectrum given the three discernible proton groups, of which notably the CH_3 and CH_2 groups are sufficiently close to have split peaks caused by J coupling. As the focus is on low-frequency measurements, we aim to measure the peaks of the CH_3 group, which are shifted to around 14 Hz. The readout signal is shown in Fig. 5(b), and the amplitudes of the three low-frequency signals (7, 14, and 21 Hz) are 9.6, 19.7, and 13.6 nT initially, and decay to 0.4, 0.9, and 0.6 nT in 0.27 s with $T_2^* \approx 0.2$ s. The roughly 1:2:1 structure in amplitude with a peak-to-peak difference of 7 Hz is in good agreement with the known J-coupling value of ethanol's CH_3 group ($^3J_{\mathrm{H,H}} = 6.9$ Hz [31]).

III. DISCUSSION

To compare our results with the standard coherent method for measuring ac fields, the Hahn-echo sequence [32], we use the results of the single N-V center with the longest coherence time published so far [3], as this allows measurement of the lowest frequency. The frequency dependency of this sensitivity is added to Fig. 3(a). Naturally, since our fitting-based algorithm needs at least several data points each period while the Hahn-echo measurement requires just one, our sensitivity at higher frequencies is worse compared to the Hahn-echo measurement. However, the Hahn-echo sensitivity at low frequencies becomes exponentially worse due to a finite T_2 (2.4 ms). The threshold frequency is about 0.36 kHz.

As an alternative, we analyze the measurement data by applying the Fourier transform and fitting a Lorentzian to find the amplitudes, which is a common way to process the frequency spectrum [29]. As this is rather sensitive to the noise near the single sharp peak (see Sec. VI within the Supplemental Material [27]), the uncertainties vary greatly; the example in Sec. VI within the Supplemental Material [27] is the most common case. Hence, to get an impression of the low-frequency amplitude sensitivity, the mean of the sensitivities for the long measurements times (thus the noise is averaged for longer) is added to Fig. 3(a). Although the sensitivity is significantly worse compared to the one from the time-domain analysis, care should be taken when interpreting these results. Depending on the application, processing the data in the frequency domain with different methods (instead of Lorentzian fitting) could be suitable and could result in improved sensitivities. Nonetheless, when looking at the spectral resolution, time-domain fitting methods, such as harmonic inversion [33], which finds the frequency and amplitude of K combined cosines given N data points, have an in principle "infinite" frequency resolution, thus the Fourier transform seems lacking with a T^{-1} spectral resolution. Once again, since both domains do contain all information, it might be possible to extract the same spectral information from the frequency domain as well, but it seems that the time domain has the more convenient methods.

The dc sensitivity for our N-V center utilizing the well-known cw ODMR method [20] is drawn in Fig. 3(a) as well. It shows that the dc sensitivity is over 2 orders of magnitude worse; any low-frequency algorithm would have a sensitivity strictly worse than the dc sensitivity. This improvement is as expected, since coherence-based methods are more sensitive and benefit more from longer coherence times than noncoherence-based ones [20]. A reason is the power broadening due to the laser and the MW. When comparing with recent results of cw ODMR experiments, the sensitivity of our algorithm with a single N-V center is comparable to the sensitivity of earlier ODMR techniques with ensembles (for example, with 10^{13} N-V centers giving $\eta \approx 2.9$ nT Hz$^{-0.5}$ [9]). For fair comparison, for both techniques all overhead is included. With the single N-V center in the current experiment, a rather high spacial resolution is possible compared to ensembles. More recent ODMR techniques with ensembles have an improved sensitivity, however the lowest frequency is about 5 Hz [11], while our algorithm has no lower bound in principle. Additional technical improvements have enhanced the sensitivity even further, as for example with flux concentrators for a bandwidth of 20–200 Hz [12].

The power broadening induced by the laser can be removed by utilizing the pulsed ODMR method. However, the sensitivity is worse by a factor of $\sqrt{2e}$, with e Euler's number, and an additional reduction occurs due to a loss in contrast [20]. This theoretical sensitivity, based on the results with the Ramsey sequence (thus assuming fitting as well), is plotted in Fig. 3(a). We are not able to verify this theoretical best sensitivity for pulsed ODMR, as the contrast decreased rapidly while elongating the MW pulse. The pulsed ODMR in Sec. V within the Supplemental Material [27] utilizes a MW pulse length of 1.5 μs, which is still orders of magnitude away from the optimum around T_2^* [20]. Likely, this is a technical limitation only. Nonetheless, compared to our results with the Ramsey sequence, the sensitivity is worse. Moreover, the range of measurable field amplitudes is significantly lower, since this is limited by the line width of the pulsed ODMR spectrum, hence a measurement such as in Fig. 2(d) would not be possible.

Besides measuring the ac amplitude of a field, the dc component, the phase and potentially the frequency (for measurements using synchronization only) follow as well (see Sec. IV within the Supplemental Material [27]). For the dc component, although it follows from fitting, the sensitivity is the same as expected from its standard method (a single fixed-delay FID sequence [26]). This is intuitive, since within the same measurement time, the sequence is repeated the same number of times for both. Moreover, for this algorithm, the ac sensitivity shows to be about $\sqrt{2}$ worse than the dc sensitivity, as is expected from theory (see Sec. I within the Supplemental Material [27]). The intuition is that for fitting a constant, a single data point suffices, while fitting an amplitude, which essentially is a difference between two points, requires double the points. Since, as mentioned before, $\eta \propto N^{-0.5}$, this gives the factor of $\sqrt{2}$.

Although the linear regime of the algorithm is investigated so far to compare with other methods, it can be extended to work outside this regime. This allows measurement with a higher dynamic range, as, for example, shown in Fig. 2(d). Multiple readout phases are required (this is possible via changing the phase of the MW pulses), and the resulting sensitivity is $\sqrt{2}$ worse compared to just measuring in the linear regime (see Sec. VII within the Supplemental Material for details [27]). Note that the latter is an effect expected for increased dynamic range measurements [25], it is not a direct effect of the low-frequency algorithm itself.

We exhibit the working of our algorithm at a field 2 orders of magnitude lower than before, and in principle, it works at zero field. However, around zero field, it is in the nonlinear regime, and the sensitivity would decrease [contrary to a nonzero field offset, multiple readout phases are not possible in this case, see Fig. 4(d,e)]. Measuring at a delay-dependent field offset, for a delay of 0.2 ms it is a few tens of nT, a signal can be measured in the linear regime at a sensitivity about 1.5 times worse compared to high-field measurements, as the states with a nitrogen nuclear spin of 0 are not utilized (thus lowering the contrast) given the dependence on electrical field and strain. This is in principle sufficient for ultralow field NMR and for biomedical applications. Even at zero field, the field is only as zero as the signal that is measured. Nonetheless, from a theoretical point of view, the sensitivity at zero field while measuring a field with an amplitude of zero is negligible, since it is always at an extremum, which has zero gradient [Fig. 4(a)]. However, a neat way to circumvent this is to apply circularly polarized MW pulses [21], also possible for large areas [34], which allows to move the maximum gradient to zero field. Thus, with such technical additions, the algorithm itself works at the true zero field as well.

For demonstrating the measurement of synchronized signals, a NMR signal is chosen. Although here it is not our focus, we give a short comparison with previous N-V center NMR research [29]. There, the high-frequency NMR spectrum for water is measured with an ensemble of N-V centers resulting in a line width of 9 ± 1 Hz with a signal frequency of approximately 3.8 MHz for the free nuclear precession measurement. Opposed to the convention of standard NMR, they found their line width via a fit to the power spectrum, which decreases the line width to $\sqrt{\sqrt{2}-1} \approx 64\%$ of the conventional line width. The conventional line width for our measurement of a water sample is 1.6 Hz (see Sec. VIII within the Supplemental Material [27]), hence in principle we show an improvement by an order of magnitude. However, note that their experiment is rather different, so this does not properly reflect the methods. Ultimately, for both methods, the line width is limited by the coherence time of the NMR sample in conjunction with the noise. Since at lower fields, narrower line widths are possible under similar conditions [17], there is significant potential for our low-frequency algorithm. Although the low-frequency NMR signal is created specifically to demonstrate the synchronized measurement, as potential application we consider low-field NMR with a N-V center near the surface [35] to sense chemicals or single molecules [36].

For synchronized measurements, the sensitivity is frequency independent up to a maximum frequency. However, note that for the nonsynchronized measurements, even though the sensitivity is the same for every frequency as well, a single sequence is designed for a certain period only. By accumulating measurements over many periods, the sequence functions as a filter, where the shape depends on the number of accumulations and with maxima directly related to this period (for the base frequency and its harmonics up to a maximum). Thus, for the nonsynchronized case, the same sensitivity can be reached for any low frequency by changing the sequence accordingly.

Finally, we reflect on our method in a more general way. In principle, the measurement subsequence could be replaced by different options, and the analysis method could be replaced by alternatives, and low-frequency fields can be measured still. When it comes to the measurement subsequence, for example, pulsed ODMR could replace the Ramsey subsequence, while other promising sequences are less straightforward to use when repeating the full sequence over multiple periods, such as ones with MW frequency offsets [37]. Many choices for the analysis method exist as well. For example, there are Fourier-based methods [29] and harmonic inversion [33], which require little prior information, where harmonic inversion is more susceptible to noise but has a great spectral resolution, while Fourier is rather intuitive. On the other hand, Bayesian inference [38] requires decent prior knowledge, and excels in analyzing large data with underlying models. Fitting is somewhere in between: some prior knowledge is often helpful, it is resilient to noise, it has a decent spectral resolution, it is fairly intuitive, but the number of data points should be relatively small. The choice depends on the circumstances. In our case, we choose to use Ramsey, as it gives the best sensitivity, and we choose to analyze via fitting, which processes all data points at once, suitable for accumulated data, and in principle any periodic signal with known shape, such as a triangular wave, can be measured.

In conclusion, we demonstrate an algorithm with a frequency-independent sensitivity for measuring low-frequency fields. We show its working for ac magnetic fields, yielding a sensitivity of 9.4 nT $\mathrm{Hz}^{-0.5}$ for a single N-V center for frequencies ranging from about 0.5 kHz down to 1 Hz, and it is expected that the sensitivity remains the same at even lower frequencies. The algorithm works for any periodic low-frequency field, as essentially it works as a quantum oscilloscope, and multiple parameters, such as phase and offset, can be determined. Moreover, the algorithm works at ultralow field, here demonstrated at 30 nT, and it can be extended to zero field. As example of a synchronized signal, we measure low-frequency NMR spectra for deionized water and ethanol, showing line widths in the order of a Hz. This technique is promising for applications that require highly sensitive low-frequency quantum sensing with nanoscale resolution such as low-field NMR, magnetic resonance imaging, and diagnostic evaluation of integrated circuits.

ACKNOWLEDGMENTS

The authors acknowledge the financial support from JST OPERA (Grant No. JPMJOP1841), KAKENHI (Grant No. 21H04653) and the Collaborative Research Program of ICR, Kyoto University (2021-114).

APPENDIX: NMR SIGNAL GENERATION

The static magnetic field B_0 is generated by a thermally stabilized permanent magnet ($B_0 = 1.0$ T; Magriteck Spinsolve 43 Carbon). The rf coil for excitation and detection (swapped between via a Mini-Circuits ZYSWA-2-50DR+ switch) of nuclear spins is wound around the NMR glass tube and inserted to the NMR magnet (3.1-mm coil diameter; 8-turn solenoid; $L = 186$ nH). The sample volume surrounded by the coil is approximately 20 μl. The coil is tuned to the frequency of the proton spin (44.145 MHz) with a standard LC circuit with variable tuning and matching capacitors and the quality factor of the coil is 210.

The rf pulse is generated by an arbitrary waveform generator (Rigol DG 4102) and is typically approximately 1.5 ms long with approximately 1-mW power at the resonant frequency. The NMR signal from nuclear spins is first amplified by a factor of 100 (40 dB) by a low-noise voltage amplifier (FEMTO GmbH DHPVA-201), and then down-converted to audiofrequencies by mixing with a reference rf signal with a double-balanced mixer (R&K Co Ltd MX010-0S). This signal is further amplified by 20 dB and filtered for frequencies below 1 kHz with a second amplifier (Stanford Research SR560) before transferring to the coil around the diamond sample. This coil consists of three turns and has a conversion factor of 12.3 $\mu\mathrm{T}\ \mathrm{V}^{-1}$.

For the NMR samples, deionized water and ethanol are obtained from Fujifilm Wako Co and degassed prior to use.

[1] C. L. Degen, F. Reinhard, and P. Cappellaro, Quantum sensing, Rev. Mod. Phys. **89**, 035002 (2017).

[2] L. Rondin, J.-P. Tetienne, T. Hingant, J.-F. Roch, P. Maletinsky, and V. Jacques, Magnetometry with nitrogen-vacancy defects in diamond, Rep. Prog. Phys. **77**, 056503 (2014).

[3] E. D. Herbschleb, H. Kato, Y. Maruyama, T. Danjo, T. Makino, S. Yamasaki, I. Ohki, K. Hayashi, H. Morishita, M. Fujiwara, and N. Mizuochi, Ultra-long coherence times amongst room-temperature solid-state spins, Nat. Commun. **10**, 3766 (2019).

[4] N. Bar-Gill, L. M. Pham, A. Jarmola, D. Budker, and R. L. Walsworth, Solid-state electronic spin coherence time approaching one second, Nat. Commun. **4**, 1743 (2013).

[5] A. Stark, N. Aharon, T. Unden, D. Louzon, A. Huck, A. Retzker, U. L. Andersen, and F. Jelezko, Narrow-bandwidth sensing of high-frequency fields with continuous dynamical decoupling, Nat. Commun. **8**, 1105 (2017).

[6] J. Meinel, V. Vorobyov, B. Yavkin, D. Dasari, H. Sumiya, S. Onoda, J. Isoya, and J. Wrachtrup, Heterodyne sensing of microwaves with a quantum sensor, Nat. Commun. **12**, 2737 (2021).

[7] V. M. Acosta, A. Jarmola, E. Bauch, and D. Budker, Optical properties of the nitrogen-vacancy singlet levels in diamond, Phys. Rev. B **82**, 201202 (2010).

[8] R. S. Schoenfeld and W. Harneit, Real Time Magnetic Field Sensing and Imaging Using a Single Spin in Diamond, Phys. Rev. Lett. **106**, 030802 (2011).

[9] H. Clevenson, M. E. Trusheim, C. Teale, T. Schröder, D. Braje, and D. Englund, Broadband magnetometry and temperature sensing with a light-trapping diamond waveguide, Nat. Phys. **11**, 393 (2015).

[10] J. F. Barry, M. J. Turner, J. M. Schloss, D. R. Glenn, Y. Song, M. D. Lukin, H. Park, and R. L. Walsworth, Optical magnetic detection of single-neuron action potentials using quantum defects in diamond, Proc. Natl. Acad. Sci. **113**, 14133 (2016).

[11] J. M. Schloss, J. F. Barry, M. J. Turner, and R. L. Walsworth, Simultaneous Broadband Vector Magnetometry Using Solid-State Spins, Phys. Rev. Appl. **10**, 034044 (2018).

[12] C. Zhang, F. Shagieva, M. Widmann, M. Kübler, V. Vorobyov, P. Kapitanova, E. Nenasheva, R. Corkill, O. Rhrle, K. Nakamura, H. Sumiya, S. Onoda, J. Isoya, and J. Wrachtrup, Diamond Magnetometry and Gradiometry Towards Subpicotesla dc Field Measurement, Phys. Rev. Appl. **15**, 064075 (2021).

[13] J. W. Blanchard, M. P. Ledbetter, T. Theis, M. C. Butler, D. Budker, and A. Pines, High-resolution zero-field NMR *J*-spectroscopy of aromatic compounds, J. Am. Chem. Soc. **135**, 3607 (2013).

[14] D. A. Barskiy, M. C. D. Tayler, I. Marco-Rius, J. Kurhanewicz, D. B. Vigneron, S. Cikrikci, A. Aydogdu, M. Reh, A. N. Pravdivtsev, J.-B. Hövener, J. W. Blanchard, T. Wu, D. Budker, and A. Pines, Zero-field nuclear magnetic resonance of chemically exchanging systems, Nat. Commun. **10**, 3002 (2019).

[15] A. Garcon, J. W. Blanchard, G. P. Centers, N. L. Figueroa, P. W. Graham, D. F. Jackson Kimball, S. Rajendran, A. O. Sushkov, Y. V. Stadnik, A. Wickenbrock, T. Wu, and D. Budker, Constraints on bosonic dark matter from ultralow-field nuclear magnetic resonance, Sci. Adv. **5**, eaax4539 (2019).

[16] T. Wu, J. W. Blanchard, G. P. Centers, N. L. Figueroa, A. Garcon, P. W. Graham, D. F. J. Kimball, S. Rajendran, Y. V. Stadnik, A. O. Sushkov, A. Wickenbrock, and D. Budker, Search for Axionlike Dark Matter with a Liquid-State Nuclear Spin Comagnetometer, Phys. Rev. Lett. **122**, 191302 (2019).

[17] R. McDermott, A. H. Trabesinger, M. Mück, E. L. Hahn, A. Pines, and J. Clarke, Liquid-state NMR and scalar couplings in microtesla magnetic fields, Science **295**, 2247 (2002).

[18] D. I. Hoult and R. E. Richards, Critical factors in the design of sensitive high resolution nuclear magnetic resonance spectrometers, Proc. R. Soc. Lond. A **344**, 311 (1975).

[19] G. A. Morris, *NMR Data Processing*, Reference Module in Chemistry, Molecular Sciences and Chemical Engineering (Elsevier, 2013).

[20] A. Dréau, M. Lesik, L. Rondin, P. Spinicelli, O. Arcizet, J.-F. Roch, and V. Jacques, Avoiding power broadening in optically detected magnetic resonance of single NV defects for enhanced dc magnetic field sensitivity, Phys. Rev. B **84**, 195204 (2011).

[21] H. Zheng, J. Xu, G. Z. Iwata, T. Lenz, J. Michl, B. Yavkin, K. Nakamura, H. Sumiya, T. Ohshima, J. Isoya, J. Wrachtrup, A. Wickenbrock, and D. Budker, Zero-Field Magnetometry Based on Nitrogen-Vacancy Ensembles in Diamond, Phys. Rev. Appl. **11**, 064068 (2019).

[22] J. Cerrillo, S. Oviedo Casado, and J. Prior, Low Field Nano-NMR via Three-Level System Control, Phys. Rev. Lett. **126**, 220402 (2021).

[23] N. F. Ramsey, A molecular beam resonance method with separated oscillating fields, Phys. Rev. **78**, 695 (1950).

[24] A. Gruber, A. Dräbenstedt, C. Tietz, L. Fleury, J. Wrachtrup, and C. v. Borczyskowski, Scanning confocal optical microscopy and magnetic resonance on single defect centers, Science **276**, 2012 (1997).

[25] E. D. Herbschleb, H. Kato, T. Makino, S. Yamasaki, and N. Mizuochi, Ultra-high dynamic range quantum measurement retaining its sensitivity, Nat. Commun. **12**, 306 (2021).

[26] J. M. Taylor, P. Cappellaro, L. Childress, L. Jiang, D. Budker, P. R. Hemmer, A. Yacoby, R. Walsworth, and M. D. Lukin, High-sensitivity diamond magnetometer with nanoscale resolution, Nat. Phys. **4**, 810 (2008).

[27] See Supplemental Material at http://link.aps.org/supplemental/10.1103/PhysRevApplied.18.034058 for derivations and supportive information.

[28] H. Kato, M. Ogura, T. Makino, D. Takeuchi, and S. Yamasaki, N-type control of single-crystal diamond films by ultra-lightly phosphorus doping, Appl. Phys. Lett. **109**, 142102 (2016).

[29] D. R. Glenn, D. B. Bucher, J. Lee, M. D. Lukin, H. Park, and R. L. Walsworth, High-resolution magnetic resonance spectroscopy using a solid-state spin sensor, Nature **555**, 351 (2018).

[30] A. P. Hitchman, F. E. M. Lilley, and W. H. Campbell, The quiet daily variation in the total magnetic field: Global curves, Geophys. Res. Lett. **25**, 2007 (1998).

[31] F. A. Bovey, *NMR Data Tables for Organic Compounds* (Wiley Interscience, New York, 1967).

[32] E. L. Hahn, Spin echoes, Phys. Rev. **80**, 580 (1950).

[33] V. A. Mandelshtam and H. S. Taylor, Harmonic inversion of time signals and its applications, J. Chem. Phys. **107**, 6756 (1997).

[34] V. Yaroshenko, V. Soshenko, V. Vorobyov, S. Bolshedvorskii, E. Nenasheva, I. Kotel'nikov, A. Akimov, and P. Kapitanova, Circularly polarized microwave antenna for nitrogen vacancy centers in diamond, Rev. Sci. Instrum. **91**, 035003 (2020).

[35] A. Watanabe, T. Nishikawa, H. Kato, M. Fujie, M. Fujiwara, T. Makino, S. Yamasaki, E. D. Herbschleb, and N. Mizuochi, Shallow NV centers augmented by exploiting n-type diamond, Carbon **178**, 294 (2021).

[36] M. Kost, J. Cai, and M. B. Plenio, Resolving single molecule structures with nitrogen-vacancy centers in diamond, Sci. Rep. **5**, 11007 (2015).

[37] A. C. Vutha and E. A. Hessels, Frequency-offset separated oscillatory fields, Phys. Rev. A **92**, 052504 (2015).

[38] I. Hincks, C. Granade, and D. G. Cory, Statistical inference with quantum measurements: methodologies for nitrogen vacancy centers in diamond, New J. Phys. **20**, 013022 (2018).

[39] J. R. Maze, P. L. Stanwix, J. S. Hodges, S. Hong, J. M. Taylor, P. Cappellaro, L. Jiang, M. V. G. Dutt, E. Togan, A. S. Zibrov, A. Yacoby, R. L. Walsworth, and M. D. Lukin, Nanoscale magnetic sensing with an individual electronic spin in diamond, Nature **455**, 644 (2008).

[40] P. Jamonneau, M. Lesik, J. P. Tetienne, I. Alvizu, L. Mayer, A. Dréau, S. Kosen, J.-F. Roch, S. Pezzagna, J. Meijer, T. Teraji, Y. Kubo, P. Bertet, J. R. Maze, and V. Jacques, Competition between electric field and magnetic field noise in the decoherence of a single spin in diamond, Phys. Rev. B **93**, 024305 (2016).